Colour flux-tubes and resonances in tetraquark systems

Pedro Bicudo, Nuno Cardoso and Marco Cardoso

CFTP, Departamento de Física, Instituto Superior Técnico,
Universidade Técnica de Lisboa, Av. Rovisco Pais, 1049-001 Lisboa, Portugal

[arXiv:1107.1355] to be published in PRD, and [arXiv:1010.0281] PRD83,094010,2011

33rd International School on Nuclear Physics, Erice, Sicilia, 18th of September 2011

Abstract

The colour fields created by the static tetraquark and pentaquark systems are computed in quenched SU(3) lattice QCD, with gauge invariant lattice operators, in a $24^3 \times 48$ lattice at $\beta = 6.2$. We generate our quenched configurations with GPUs, and detail the respective benchmanrks in different SU(N) groups. While at smaller distances the coulomb potential is expected to dominate, at larger distances it is expected that fundamental flux tubes, similar to the flux-tube between a quark and an antiquark, emerge and confine the quarks. In order to minimize the potential the fundamental flux tubes should connect at 120o angles. We compute the square of the colour fields utilizing plaquettes, and locate the static sources with generalized Wilson loops and with APE smearing. The tetraquark system is well described by a double-Y-shaped flux-tube, with two Steiner points, but when quark-antiquark pairs are close enough the two junctions collapse and we have an X-shaped flux-tube, with one Steiner point. We also indicate how to solve the Schrödinger equation for the tetraquark, a three coordinate (9 variable) system, and suggest that tetraquark resonances do exist.

Contents

.

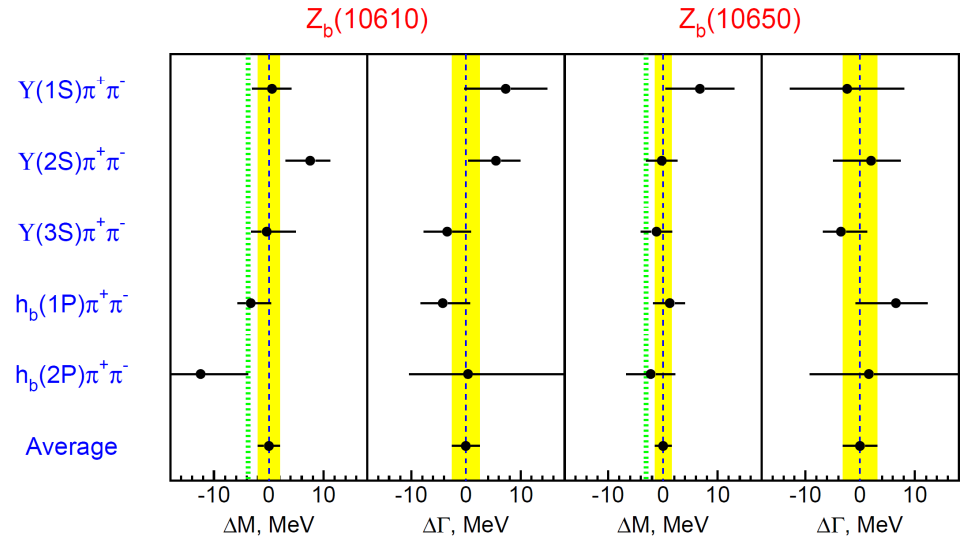

FIG. 11: Comparison of $Z_b(10610)$ and $Z_b(10650)$ parameters obtained from different decay channels. The vertical dotted lines indicate $B^*\overline{B}$ and $B^*\overline{B}^*$ thresholds.

Figure 1: Belle tetraquark candidates $Z_b^+(10610)$ and $Z_b^+(10650)$.

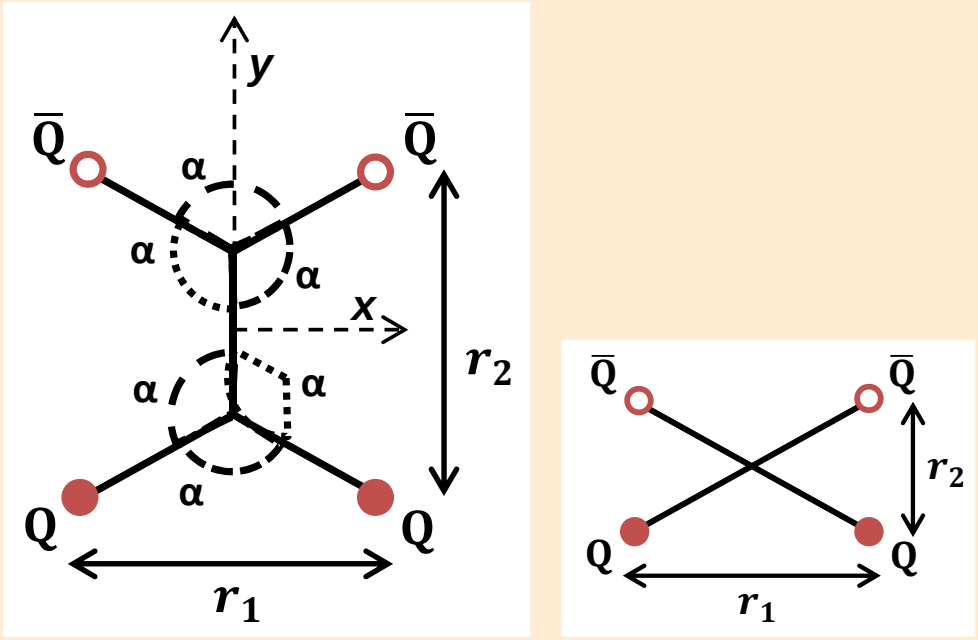

(a) (b)

Figure 2: In the tetraquark flux tube (or string) model, the elementary flux tubes meet in two Fermat points, at an angle of $\alpha = 120°$ to form a double-Y flux tube, except when this is impossible and the flux tube is X-shaped. In this model, when $r_2 > \sqrt{3}r_1$ the tetraquark flux tube minimizes the energy, and when $r_2 < \sqrt{3}r_1$ the meson-meson minimizes the energy.

1) Motivation

Multiquark exotic hadrons like the tetraquark and the pentaquark, different from the the ordinary mesons and baryons, have been studied and searched for many years. The tetraquark was initially proposed by Jaffe [1] as a bound state formed by two quarks and two antiquarks. Presently several observed resonances are tetraquark candidates. The most recent tetraquark candidates have been reported by the Belle Collaboration in May, the charged bottomonium $Z_b^+(10610)$ and $Z_b^+(10650)$ [2]. However a better understanding of tetraquarks is necessary to confirm or disprove the X, Y and possibly also light resonances candidates as tetraquark states.

On the theoretical side, the first efforts have been to search for bound states below the strong decay threshold [3, 4, 5, 6], as it is apparent that the absence of a potential barrier may produce a large decay width to any open channel. Recent investigations found that, even above the strong decay threshold, the presence of a centrifugal barrier in high angular momentum multiquarks may increase the stability of the system [7, 8].

In the last years, the static tetraquark potential has been studied in Lattice QCD computations [9, 10, 11]. The authors concluded that

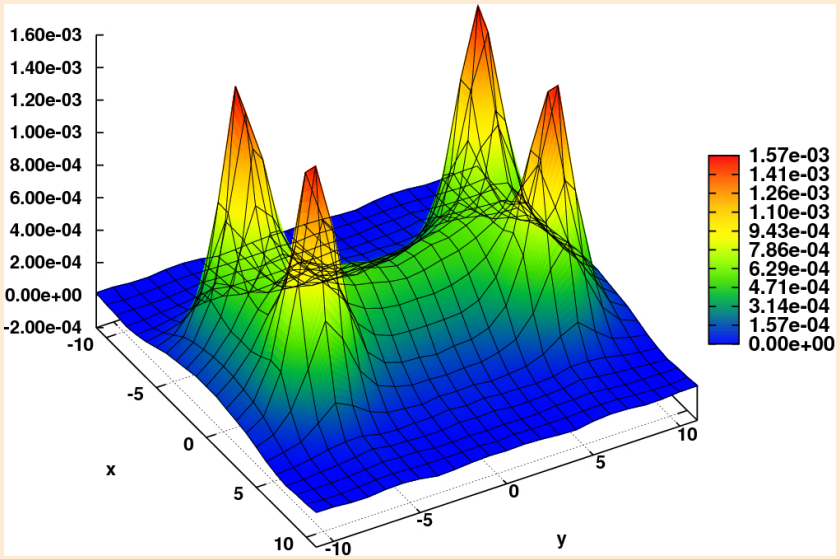

(a)

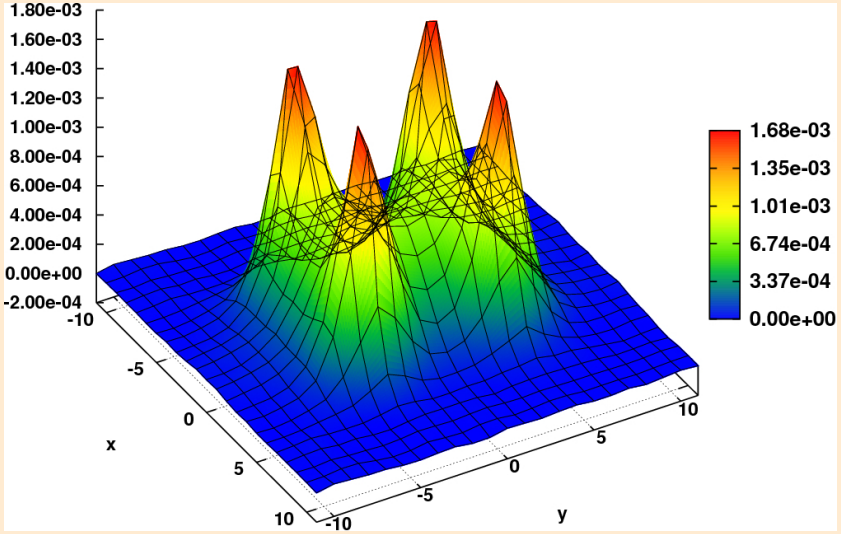

(b)

Figure 3: (a) Lagrangian density 3D plot for $r_1 = 8,\ r_2 = 14$. (b) We also show the 3D plot for $r_1 = 8$ and $r_2 = 8$, to illustrate that even at distances where the meson meson dominates the flip-flop potential, the meson meson mixing with the tetraquark is sufficiently small to produce such a clear a tetraquark double-Y flux tube. The results are presented in lattice spacing units (colour online).

when the quark-quark are well separated from the antiquark-antiquark, the tetraquark potential is consistent with One Gluon Exchange Coulomb potentials plus a four-body confining potential, suggesting the formation of a double-Y flux tube, as in Fig. 2, composed of five linear fundamental flux tubes meeting in two Fermat points [6, 12, 13]. A Fermat, or Steiner, point is defined as a junction minimizing the total length of strings, where linear individual strings join at 120° angles. When a quark approaches an antiquark, the minimum potential changes to a sum of two quark-antiquark potentials, which indicates a two meson state. In principle a X-shaped flux-tube as in Fig. 2b could also occur, but the potential minimization always leads in that case to a two-meson potential. This is consistent with the triple flip-flop potential, minimizing the length, with either tetraquark flux tubes or meson-meson flux tubes, of thin flux tubes connecting the different quarks or antiquarks [6, 8].

Here we study the colour fields for the static tetraquark system, with the aim of observing the tetraquark flux tubes suggested by these static potential computations. The study of the colour fields in a tetraquark is important to discriminate between different multi-quark Hamiltonian models. Unlike the colour fields of simpler few-body systems, say mesons, baryons and hybrids, [14, 15, 16, 17], the tetraquark fields have not been previously studied in lattice QCD.

.

2) *en passant:* Generating configurations with GPUs

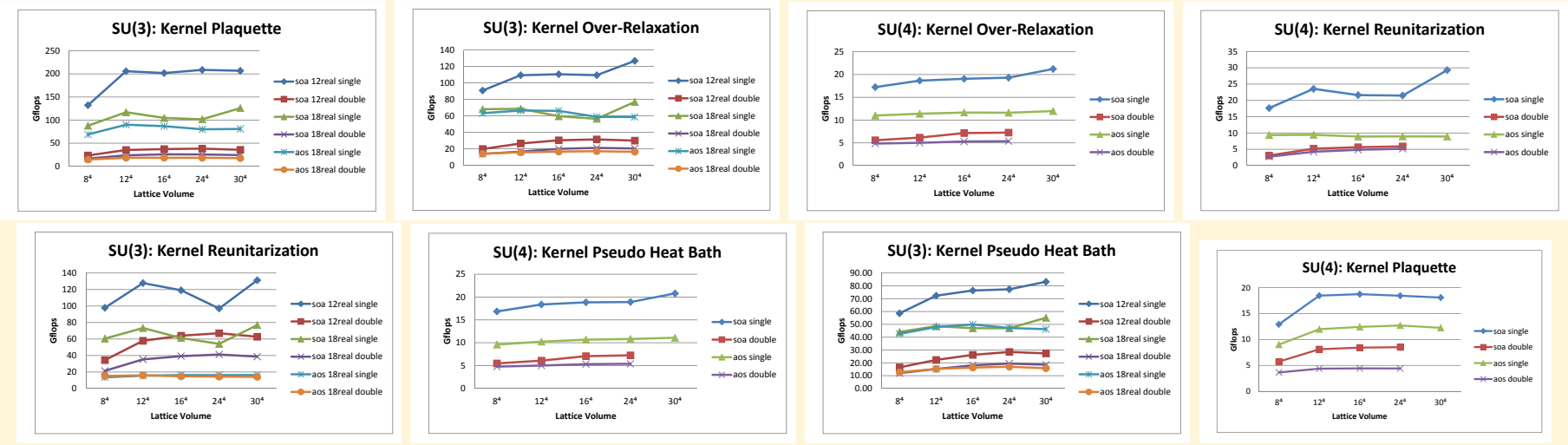

Figure 4: Benchmarks with the NVIDIA 295 GTX (NVIDIA 200 generation). The results are presented in lattice spacing units (colour online).

To produce the results presented in this work , we use 1121 quenched configurations in a $24^3 \times 48$ lattice at $\beta = 6.2$. To test whether these configurations are already close to the continuum limit, we first compare the quark-antiquark static potential obtained using these configurations with the potential of 381 configurations in a larger, $32^3 \times 64$ lattice, at the same β. The resulting quark-antiquark static potentials are identical within the statistical error, showing that the volume size effects are sufficiently small in our $24^3 \times 48$ lattice. We present our results in lattice spacing units of a, with $a = 0.07261(85)$ fm or $a^{-1} = 2718 \pm 32$ MeV. We generate our configurations in NVIDIA GPUs of the FERMI series (480, 580 and Tesla 2070) with a SU(3) CUDA code upgraded from our SU(2) combination of Cabibbo-Marinari pseudoheatbath and over-relaxation algorithm [18, 19]. Our SU(3) updates involve three SU(2) subgroups, we work with 9 complex numbers, and we reunitarize the matrix. We have two options to save the configurations, either in a structure of arrays where each array lists a given complex component for all the lattice sites, or in an array of structures where each structure is a SU(3) matrix.

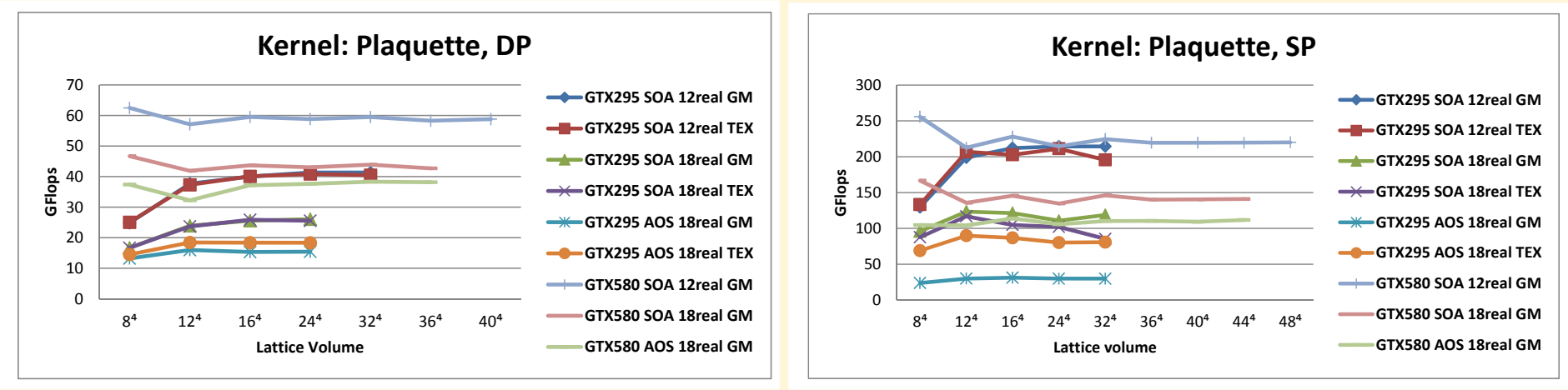

Figure 5: Comparing benchmarks for NVIDIA 295 GTX and 580 GTX boards, respectively from the 200 and Fermi generations. The results are presented in lattice spacing units (colour online).

Table 1: Memory Load per Thread

Kernel per thread	**SU(3)** 18 reals	Single/Double (bytes)	**SU(3)** 12 reals	Single/Double (bytes)	**SU(4)** 32 reals	Single/Double (bytes)
PHB and OVR per link	342	1368/2736	228	912/1824	608	2431/4864
REU per site	72	288/576	48	192/384	128	512/1024
PLAQ per site	432	1728/3456	288	1152/2304	768	3072/6144

Table 2: Performance GFlops in a 24^4 lattice.

SU(3) Single Precision	PHB	OVR	REU	PLAQ
GTX580 SOA 12real Cache	140.3	160.5	250.3	214.6
GTX295 SOA 12real GobalM	75.4	106.2	99.3	214.4
GTX295 SOA 12real TexM	78.2	109.9	97.6	211.2
GTX580 SOA 18real Cache	88.5	98.7	148.5	134.7
GTX295 SOA 18real GobalM	44.5	54.2	53.6	110.7
GTX295 SOA 18real TexM	47.0	56.3	54.4	102.1
GTX580 AOS 18real Cache	62.6	64.7	49.0	105.7
GTX295 AOS 18real GobalM	19.2	22.1	13.3	29.9
GTX295 AOS 18real TexM	47.1	58.9	16.3	80.2

SU(3) Double Precision	PHB	OVR	REU	PLAQ
GTX580 SOA 12real Cache	40.8	40.2	124.3	58.8
GTX295 SOA 12real GobalM	26.4	31.7	55.6	41.3
GTX295 SOA 12real TexM	28.5	31.8	60.4	40.8
GTX580 SOA 18real Cache	30.3	29.6	53.1	43.0
GTX295 SOA 18real GobalM	16.8	19.4	39.2	26.1
GTX295 SOA 18real TexM	19.4	21.1	41.2	25.5
GTX580 AOS 18real Cache	29.4	28.9	23.4	37.6
GTX295 AOS 18real GobalM	11.6	13.0	10.8	15.4
GTX295 AOS 18real TexM	17.0	17.1	14.5	18.4

Table 3: Performance for the PSeudoHeatBath, OVeRrelaxation, REUnitarization and PLAQuette. SOA and AOS stand respectively for structure of arrays and array of structures.

SU(4) Single Precision	PHB	OVR	REU	PLAQ
GTX580 SOA Cache	32.9	34.0	59.2	34.3
GTX295 SOA GobalM	18.2	18.3	21.7	17.6
GTX295 SOA TexM	18.9	19.4	21.4	18.7
GTX580 AOS Cache	31.4	32.6	18.2	26.4
GTX295 AOS GobalM	7.6	8.2	5.8	9.0
GTX295 AOS TexM	10.8	11.6	9.0	12.8

SU(4) Double Precision	PHB	OVR	REU	PLAQ
GTX580 SOA Cache	13.9	13.5	10.5	18.3
GTX295 SOA GobalM	7.3	7.5	5.8	9.0
GTX295 SOA TexM	7.2	7.2	5.9	8.5
GTX580 AOS Cache	12.8	12.4	6.6	13.8
GTX295 AOS GobalM	4.8	5.0	3.7	4.6
GTX295 AOS TexM	5.4	5.4	5.1	4.4

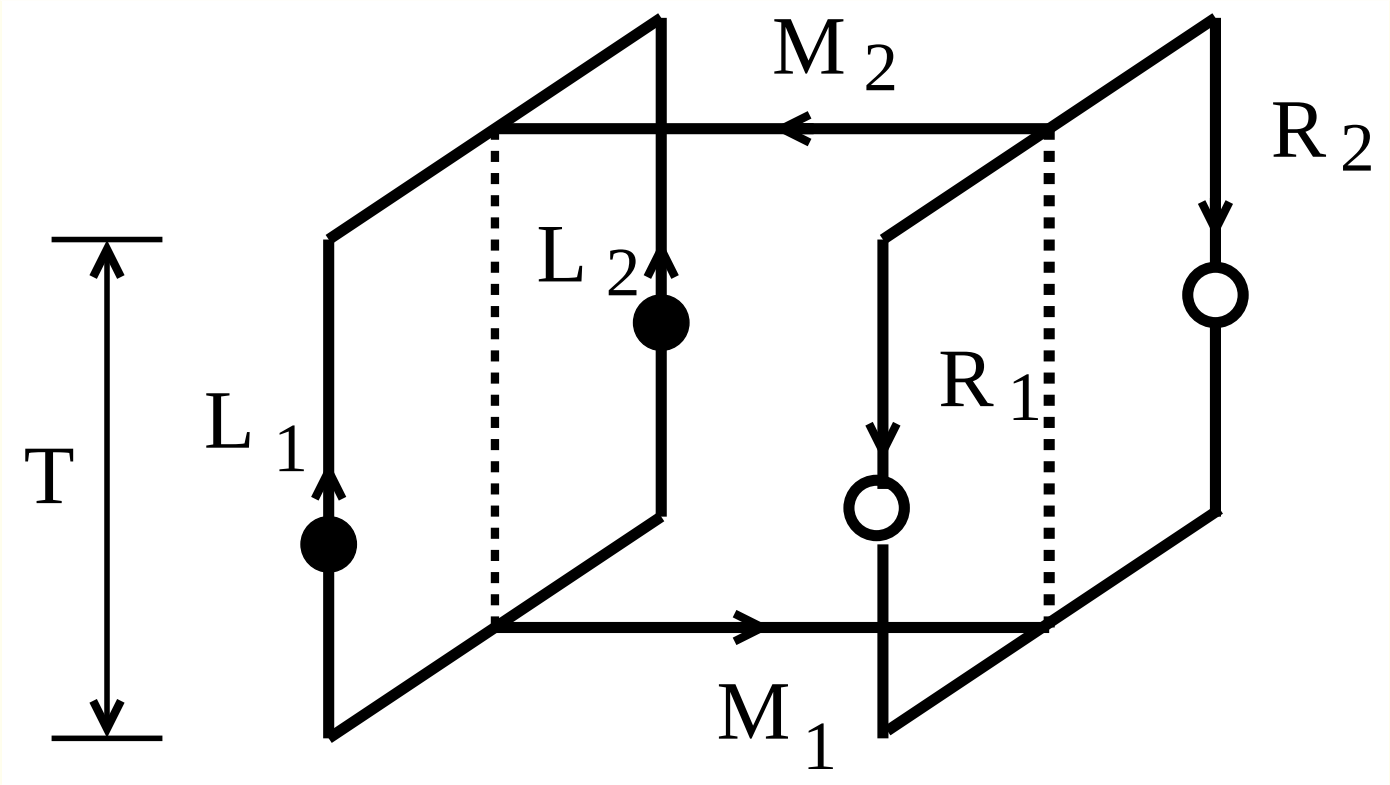

Figure 6: Tetraquark Wilson loop as defined by Alexandrou et al [9], and by Okiharu et al [10].

3) Computing Fields with the Wilson loop and the Plaquette

To impose a static tetraquark, we utilize the respective Wilson loop [9, 10] of Fig. 6, given by $W_{4Q} = \frac{1}{3}\mathrm{Tr}\,(M_1 R_{12} M_2 L_{12})$, where

$$\begin{aligned} R_{12}^{aa'} &= \frac{1}{2}\epsilon^{abc}\epsilon^{a'b'c'} R_1^{bb'} R_2^{cc'} \ , \\ L_{12}^{aa'} &= \frac{1}{2}\epsilon^{abc}\epsilon^{a'b'c'} L_1^{bb'} L_2^{cc'} \ . \end{aligned} \tag{1}$$

The chromoelectric and chromomagnetic fields on the lattice are given by the Wilson loop and plaquette expectation values,

$$\begin{aligned} \left\langle E_i^2(\mathbf{r}) \right\rangle &= \langle P(\mathbf{r})_{0i} \rangle - \frac{\langle W(r_1, r_2, T)\, P(\mathbf{r})_{0i} \rangle}{\langle W(r_1, r_2, T) \rangle} \\ \left\langle B_i^2(\mathbf{r}) \right\rangle &= \frac{\langle W(r_1, r_2, T)\, P(\mathbf{r})_{jk} \rangle}{\langle W \rangle\,(r_1, r_2, T)} - \langle P(\mathbf{r})_{jk} \rangle \ , \end{aligned} \tag{2}$$

where the jk indices of the plaquette complement the index i of the magnetic field, and where the plaquette at position $\mathbf{r} = (x, y, z)$ is computed at $t = T/2$,

$$P_{\mu\nu}(\mathbf{r}) = 1 - \frac{1}{3}\mathrm{Re}\,\mathrm{Tr}\left[U_\mu(\mathbf{r}) U_\nu(\mathbf{r}+\mu) U_\mu^\dagger(\mathbf{r}+\nu) U_\nu^\dagger(\mathbf{r})\right] \ . \tag{3}$$

The energy ($\mathcal{H}$) and lagrangian ($\mathcal{L}$) densities are then computed from the fields,

$$\langle \mathcal{H}(\mathbf{r}) \rangle = \frac{1}{2}\left(\left\langle \mathbf{E}^2(\mathbf{r}) \right\rangle + \left\langle \mathbf{B}^2(\mathbf{r}) \right\rangle\right) \ , \tag{4}$$

$$\langle \mathcal{L}(\mathbf{r}) \rangle = \frac{1}{2}\left(\left\langle \mathbf{E}^2(\mathbf{r}) \right\rangle - \left\langle \mathbf{B}^2(\mathbf{r}) \right\rangle\right) \ . \tag{5}$$

To compute the static field expectation value, we plot the expectation value $\langle E_i^2(\mathbf{r}) \rangle$ or $\langle B_i^2(\mathbf{r}) \rangle$ as a function of the temporal extent T of the Wilson loop. At sufficiently large T, the groundstate corresponding to the studied quantum numbers dominates, and the expectation value tends to a horizontal plateau. In order to improve the signal to noise ratio of the Wilson loop, we use 50 iterations of APE Smearing with $w = 0.2$ (as in [16]) in the spatial directions and one iteration of hypercubic blocking (HYP) in the temporal direction. [20], with $\alpha_1 = 0.75$, $\alpha_2 = 0.6$ and $\alpha_3 = 0.3$. Note that these two procedures are only applied to the Wilson Loop, not to the plaquette. To compute the fields, we fit the horizontal plateaux obtained for each point $\mathbf{r}$ determined by the plaquette position, but we consider $z = 0$ for simplicity. For the distances r_1 and r_2 considered, we find in the range of $T \in [3, 12]$ in lattice units, horizontal plateaux with a χ^2 /dof $\in [0.3, 2.0]$. We finally compute the error bars of the fields with the jackknife method.

.

4) *en passant:* Insight in the quark-antiquark flux tube

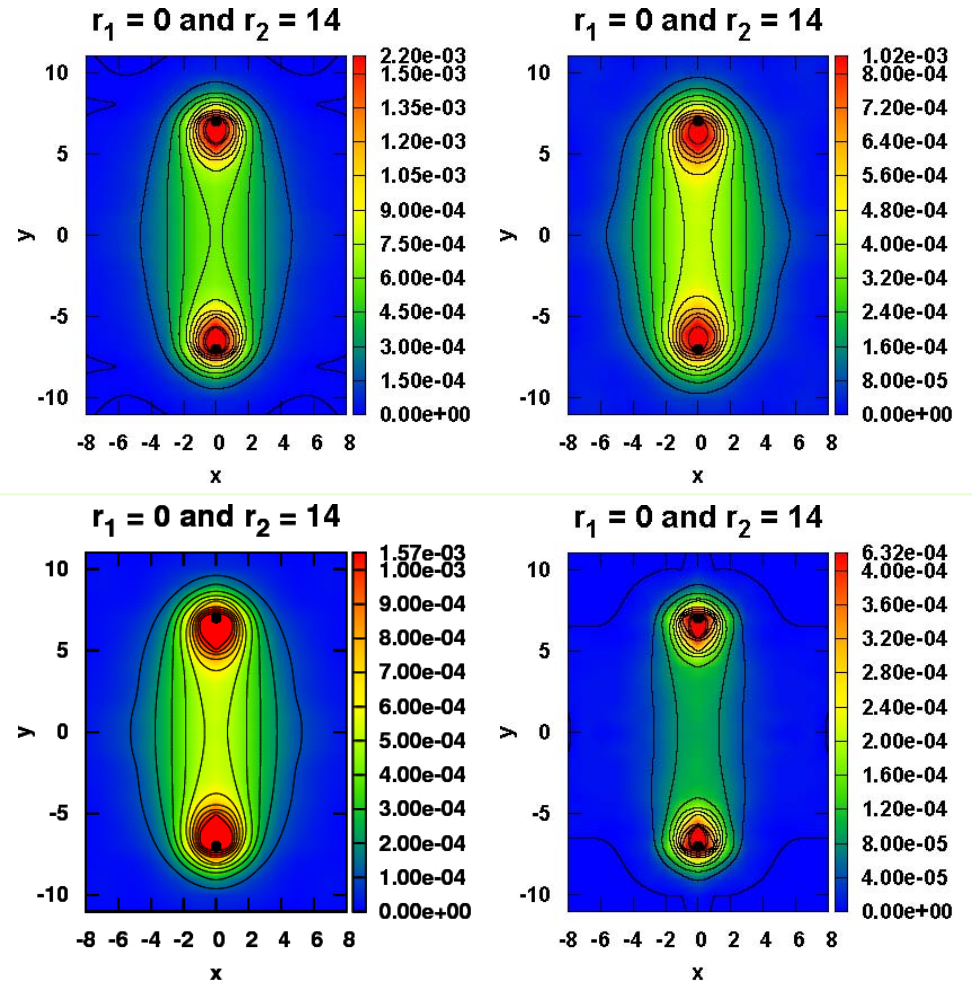

Figure 7: Density plot of the static quark-antiquark squared E and B, Lagrangian and Energy field densities for $r = 14$. The results are presented in lattice spacing units (colour online).

.

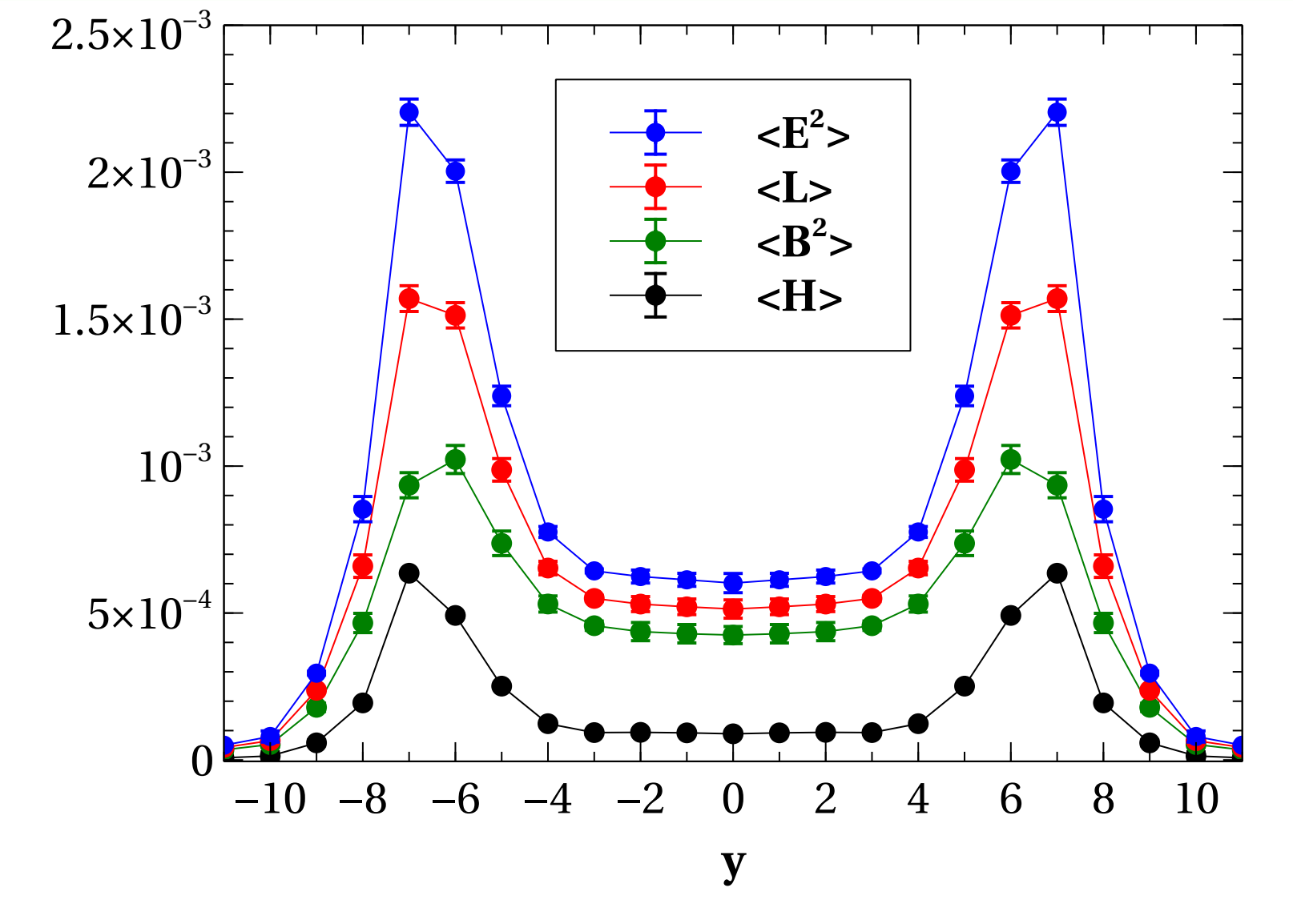

Figure 8: Cut of the fields in the longitudinal direction for $r = 14$. The results are presented in lattice spacing units (colour online).

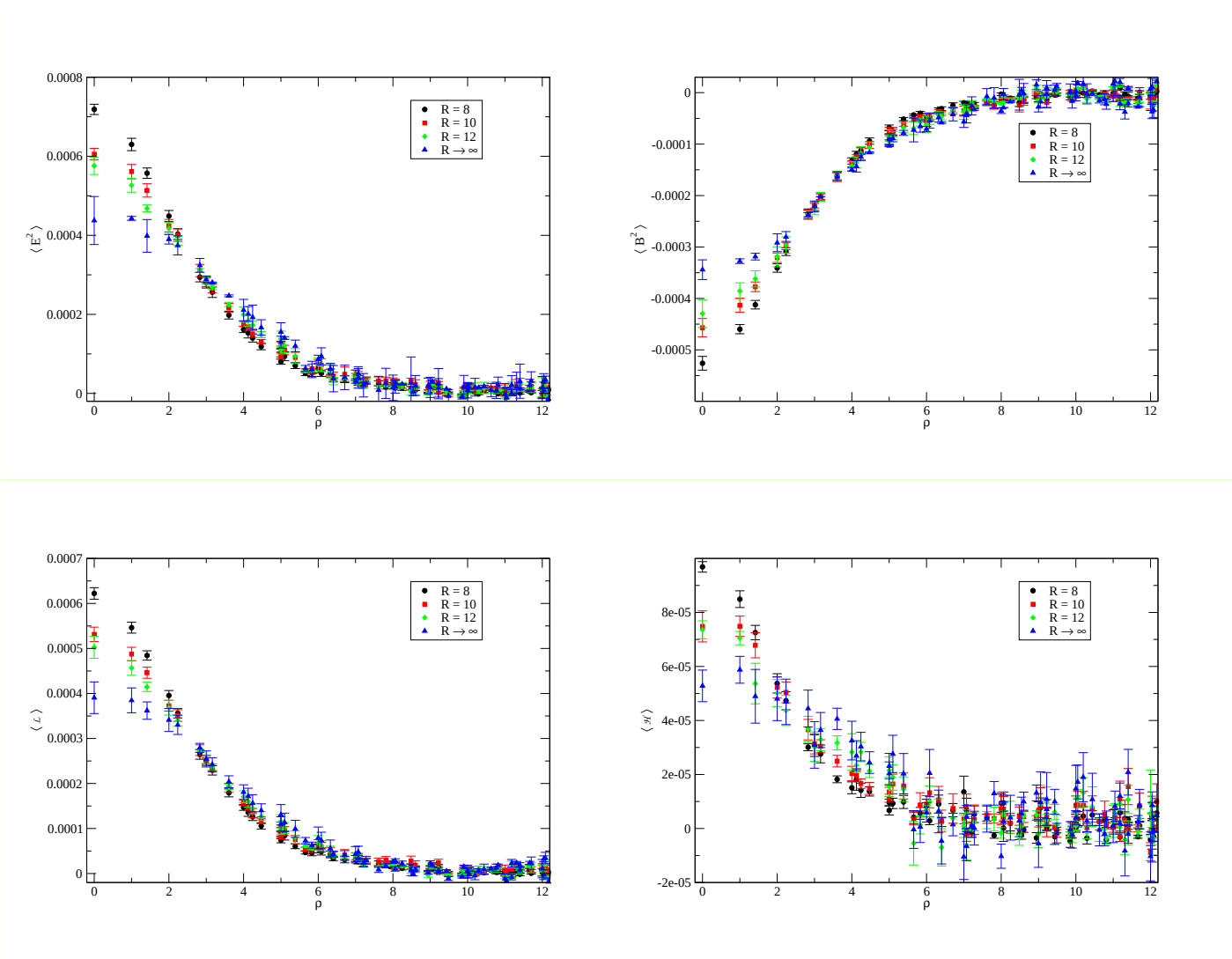

Figure 9: Perpendicular cut of the longitudinal and transversal squared components of the Electric field. and the Lagrangian and Energy densities for a static quark-antiquark. The results are presented in lattice spacing units (colour online).

5) The Tetraquark fields

In our simulations, the quarks are fixed at $(\pm\, r_1/2, -r2/2, 0)$ and the antiquarks at $(\pm\, r_1/2, r_2/2, 0)$, with r_1 extending up to 8 lattice spacing units and r_2 extended up to 14 lattice spacing units, in order to include the relevant cases where $r_2 > \sqrt{3}r_1$. Notice that in the string picture, at the line $r_2 = \sqrt{3}r_1$ in our (r_1, r_2) parameter space, the transition between the double-Y, or butterfly, tetraquark geometry in Fig. 2a to the meson-meson geometry should occur. The results are presented only for the xy plane since the quarks are in this plane and the results with $z \neq 0$ are less interesting for this study. The flux tube fields can be seen in Fig. 3, 10 and 11. Theses figures exhibit clearly tetraquark double-Y, or butterfly, shaped flux tubes. The flux tubes have a finite width, and are not infinitely thin as in the string models inspiring the Fermat points and the triple flip-flop potential, but nevertheless the junctions are close to the Fermat points, thus justifying the use of string models for the quark confinement in constituent quark models.

In Fig. **??**, we plot the chromoelectric field along the central flux tube, $\left\langle E_y^2 \right\rangle$ at $x = 0$, for $r_1 = 8$, $r_2 = 14$. As expected, the chromoelectric field along y is in agreement with the position of the Fermat points. The chromoelectric field along the $x = 0$ central axis is maximal close to the Fermat points situated at $x \simeq -4.69$ and at $x \simeq 4.69$, flattens in the middle of the flux tube. Outside the flux tube, the chromoelectric field is almost residual.

In Fig. 12, we compare the chromoelectric field for the tetraquark and the quark-antiquark system in the middle of the flux tube between the (di)quark and the (di)antiquark. As can be seen, for our larger distance $r_2 = 14$ where the source effects are small, the chromoelectric field is identical up to the error bars, and this confirms that the tetraquark flux tube is composed of a set of fundamental flux tubes with Fermat junctions.

To check which of the colour structures, tetraquark or meson-meson, produces the groundstate flux tube, we study the χ^2/dof of the T plateaux. Clearly, as expected, the X-shaped geometry of Fig. 2b never produces acceptable plateaux in the range where the meson-meson plateaux are good. But, surprisingly, event at distances as small as $r_2 \simeq \frac{1}{2} r_1 \sqrt{3}$, illustrated in Fig. 3b, where the flip-flop potential favours the two-meson flux tube, we find T plateaux with a good χ^2 /dof. This shows that the mixing between the tetraquark flux tube and the meson-meson flux tube is small, and it is possible to study clear tetraquark flux tubes even at relatively small quark-antiquark distances.

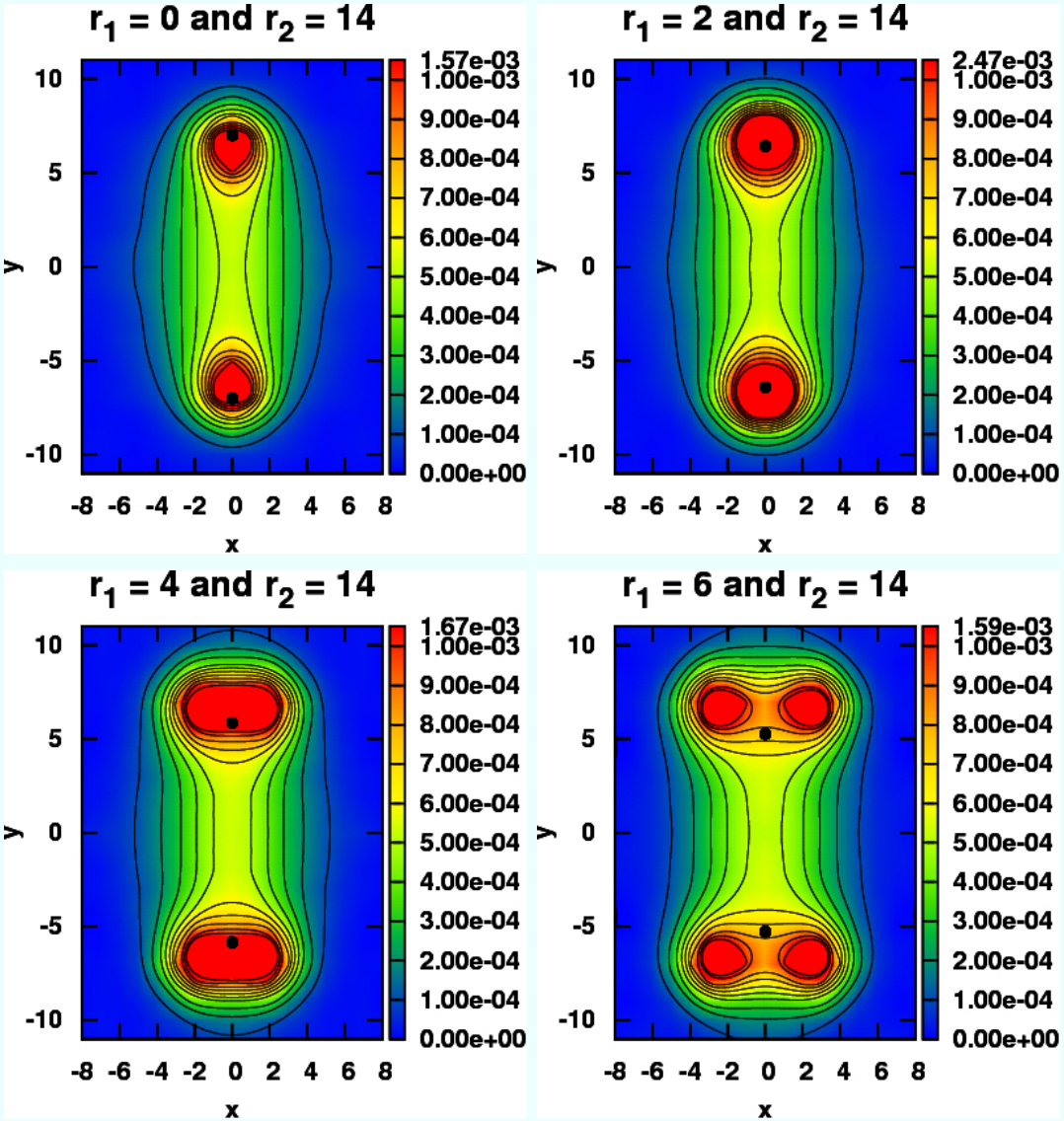

Figure 10: Lagrangian density for $r_2 = 14$ and r_1 from 0 to 6. The black dot points correspond to the Fermat points. The results are presented in lattice spacing units (colour online).

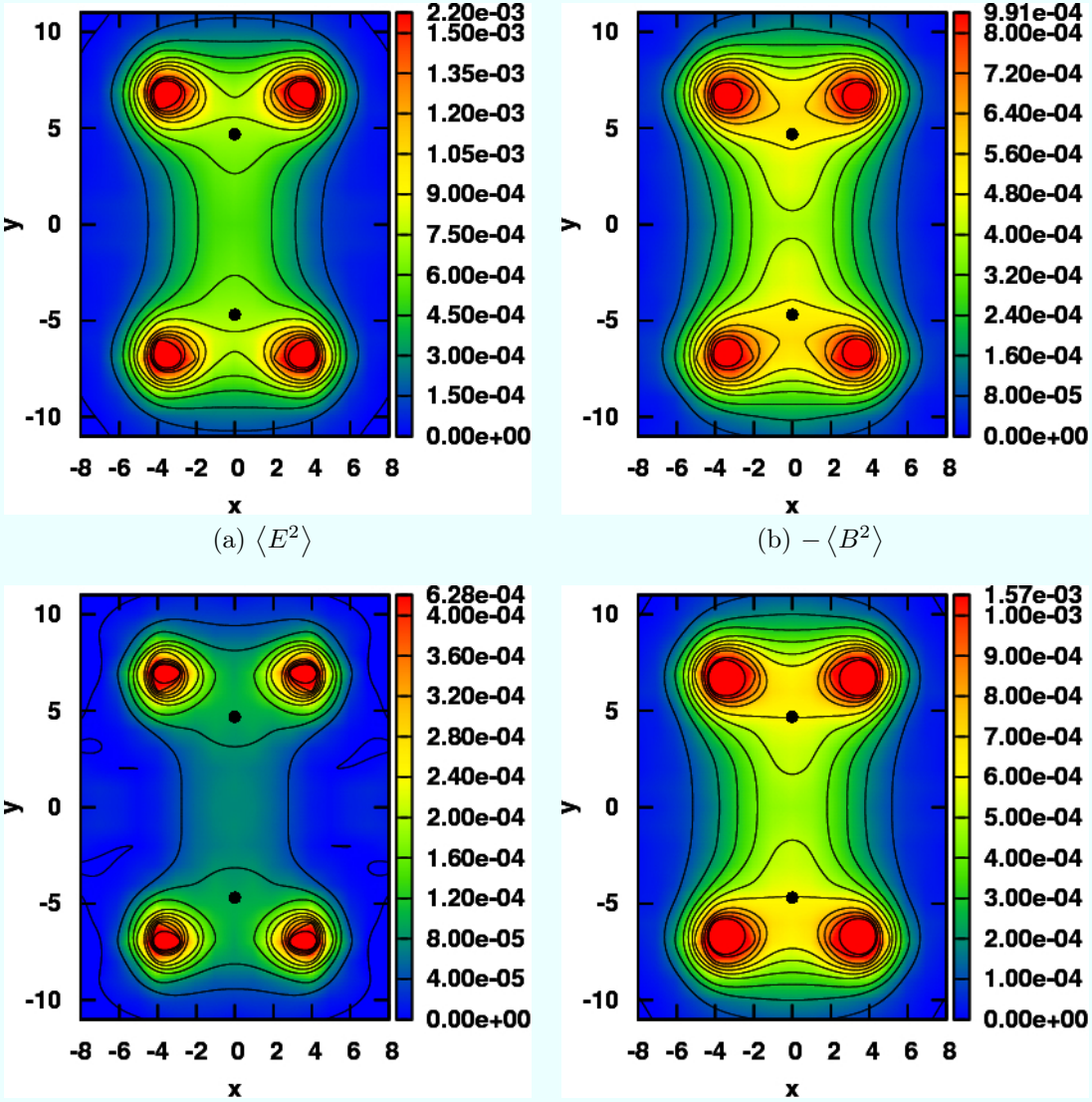

(a) $\langle E^2 \rangle$

(b) $-\langle B^2 \rangle$

(c) Energy Density

(d) Lagrangian Density

Figure 11: Colour fields, energy density and Lagrangian density for $r_1 = 8$ and $r_2 = 14$. The black dot points correspond to the Fermat points. The results are presented in lattice spacing units (colour online).

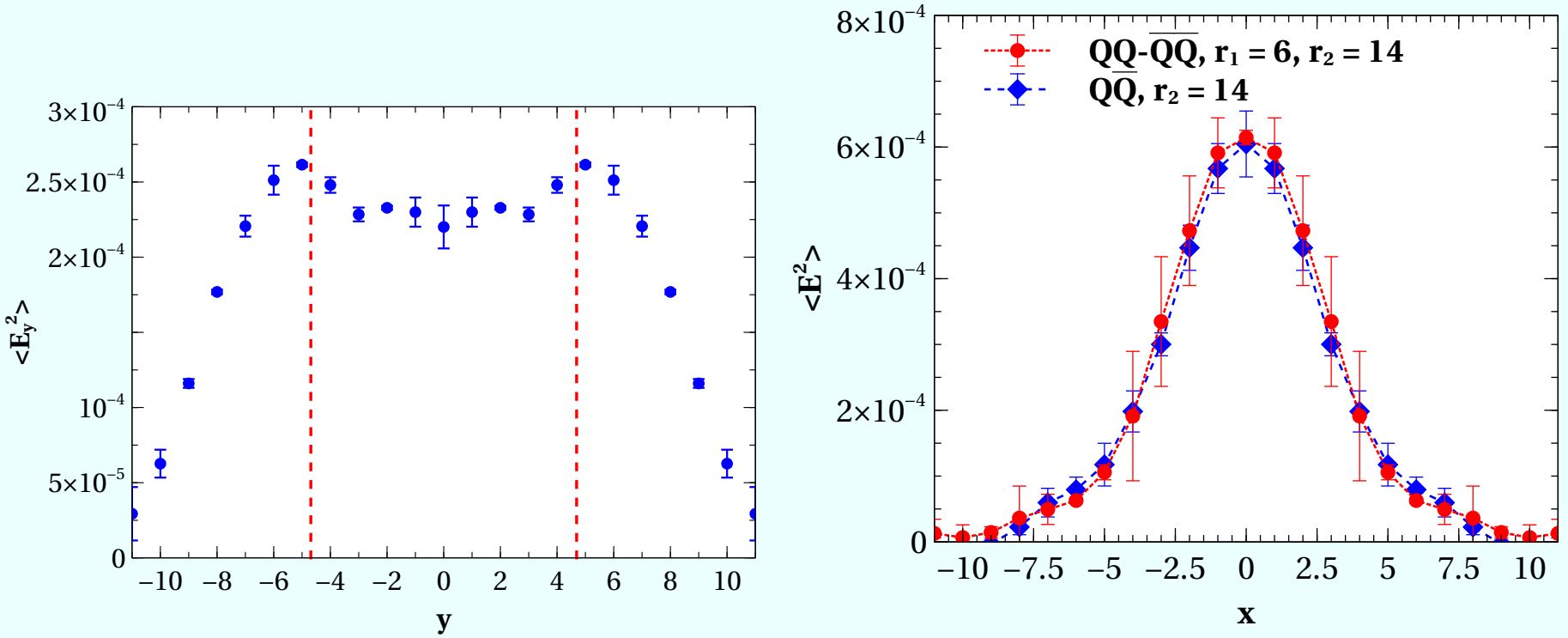

Figure 12: $\langle E_y^2 \rangle$ in the central axis $x = 0$ for $r_1 = 8,\ r_2 = 14$. We show with vertical dashed lines the location of the two Fermat points. Profile cut at $y = 0$ of the chromoelectric field for the tetraquark and quark-antiquark systems in the middle of the flux tube. The results are presented in lattice spacing units (colour online).

.

6) *en passant:* Computing phase shifts for approximate 2-coordinate tretaquarks

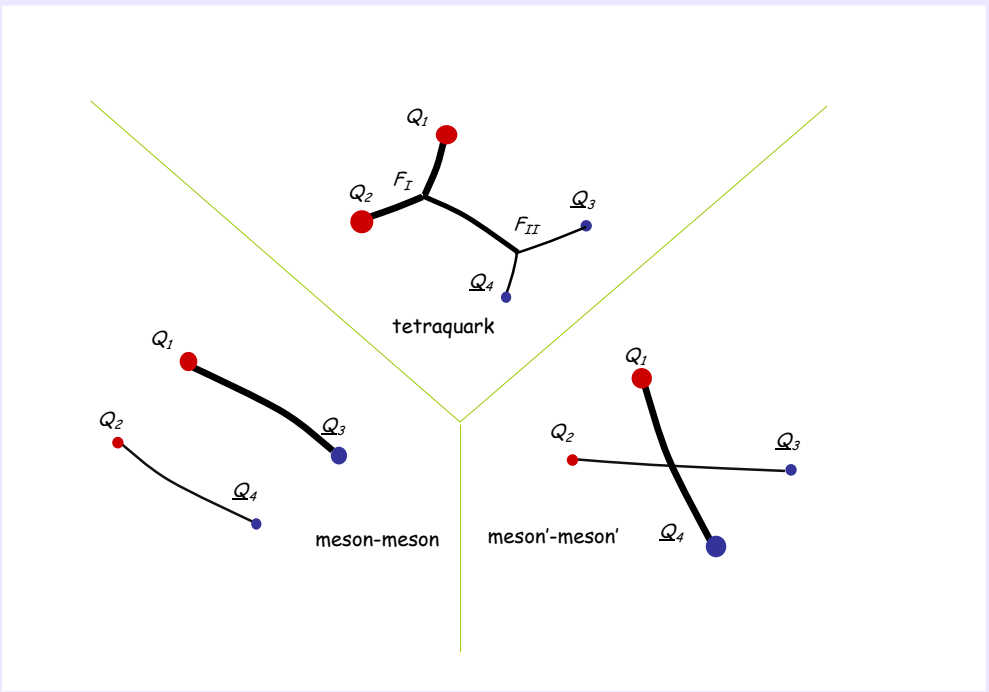

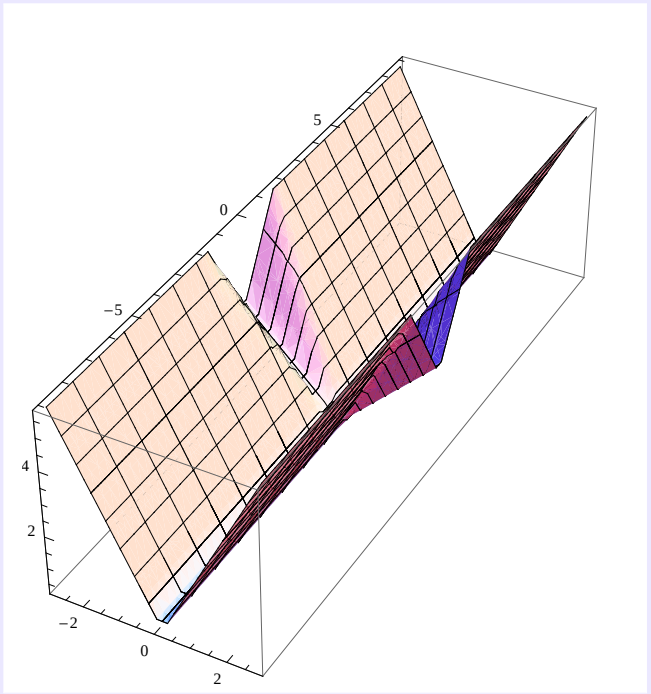

Figure 13: Triple flip-flop Potential potential. To the list of potentials to minimize including usually only two different meson pair potentials, we join another potential, the tetraquark potential. We also show the plot of our simplified flip-flop potential, as a function of the two radial variables r (compact) and ρ (open).

Recently we developed a unitarized formalism to study tetraquarks using the triple flip-flop potential, which includes two meson-meson potentials and the tetraquark four-body potential. This can be related to the Jaffe-Wilczek and to the Karliner-Lipkin tetraquark models, where we also consider the possible open channels, since the four quarks and antiquarks may at any time escape to a pair of mesons.

We studied a simplified two-variable toy model and explore the analogy with a cherry in a glass, but a broken one where the cherry may escape from. It is quite interesting to have our system confined or compact in one variable and infinite in the other variable.

In this framework we solved the two-variable Schrödinger equation in configuration space. With the finite difference method, we compute the spectrum, we search for localized states and we attempt to compute phase shifts.

We then applied the outgoing spherical wave method to compute in detail the phase shifts and and to determine the decay widths. We

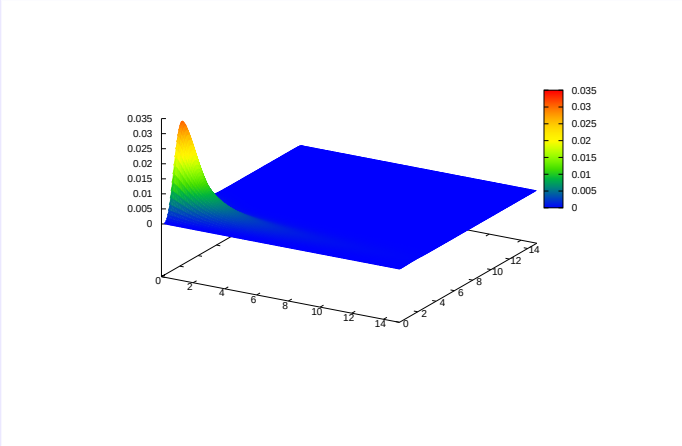

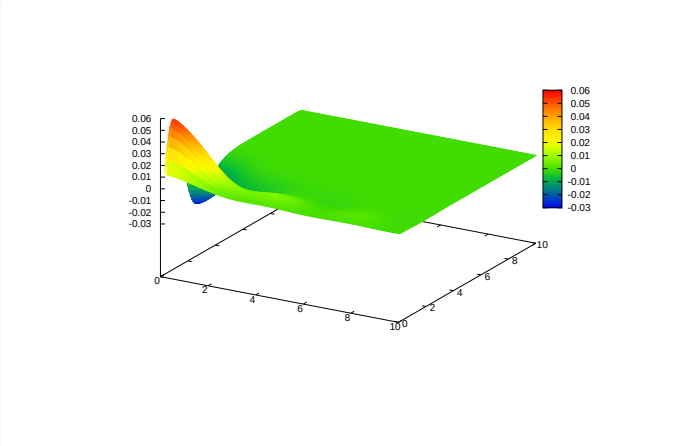

Figure 14: Among the many continuum states we may get a few localized states and semi-localized states, i e boundstates and resonances.

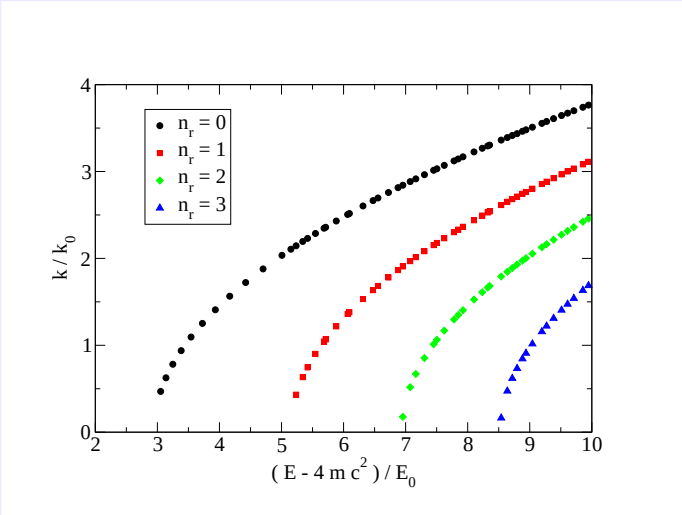

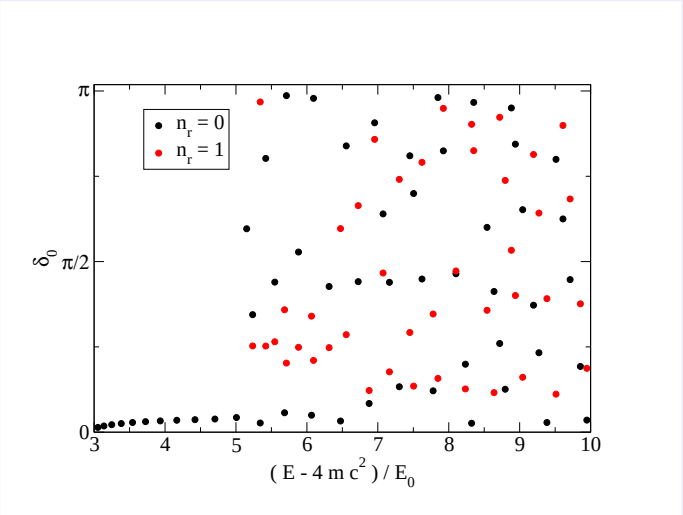

Figure 15: Momenta of the various components as a function of the energy, and "phase shifts" obtained from the finite differences (by projecting the eigenstates in the meson-meson eigenstates). As can be seen the behaviour is irregular when we have more than one channel.

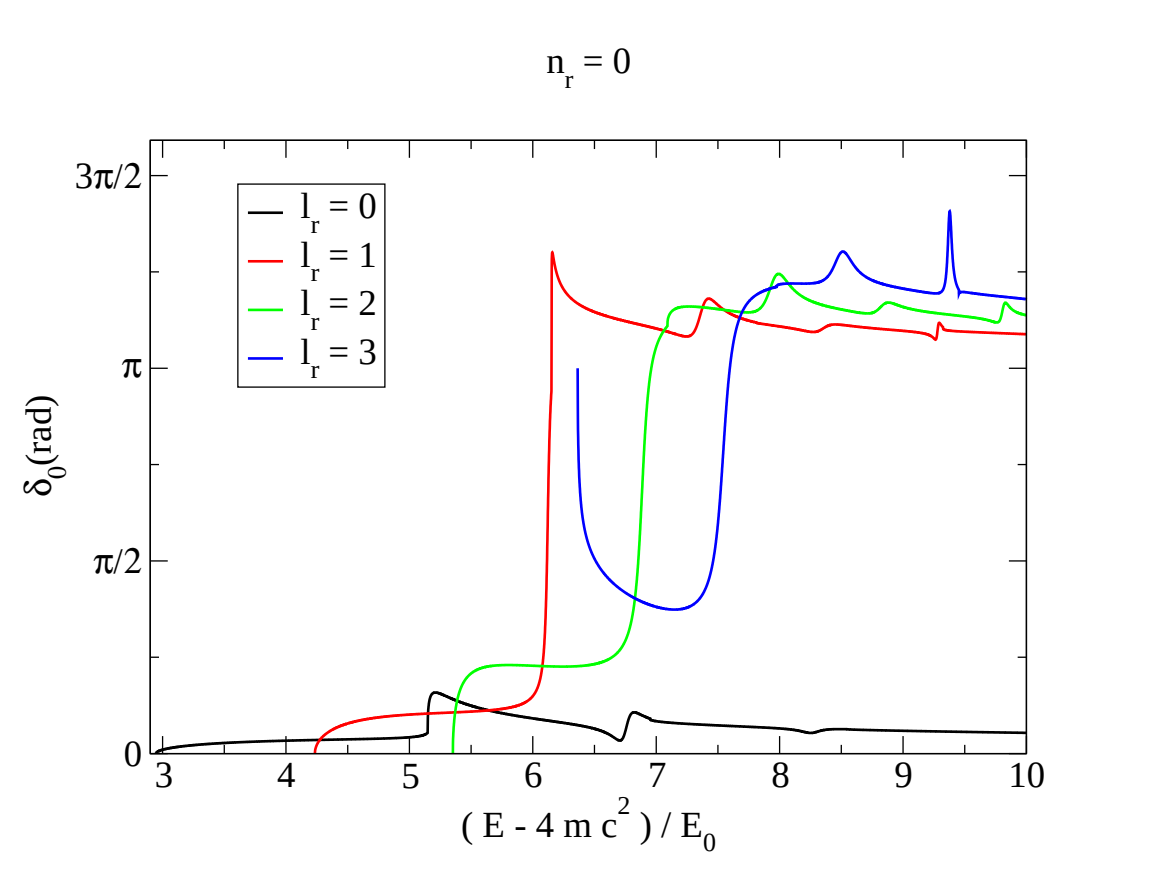

l_r	$(E-4mc^2)/E_0$	Γ / E_0
1	6.116	0.037
2	6.855	0.131
3	7.462	0.352

Figure 16: Folding the confined coordinate with the solution of the meson Schrödinger equation then we can compute with a large precision the phase shifts. Here we illustrate the case of for $l_r = 0, 1, 2$ and 3, with $n_r = 0$. We aslo show the decay widths as a function of l_r

fold the confined coordinate with the solution of the meson Schrödinger equation. We explored the model in the equal mass case, and we found narrow resonances. In particular the existence of two commuting angular momenta is responsible for our small decay widths.

.

7) Foreword

- The flux tubes remain interesting in Lattice QCD, our results support the string model of confinement, in particular for the tetraquark static potential [21].

- The mixing between the tetraquark and meson-meson flux-tubes is small, which may contribute for narrower tetraquark resonances.

- After our preliminary study of the approximate two-variable tretaquark, we are now moving on to the solutions of the Schrödinger equation for the tetraquark, in the full triple-flip-flop potential.

- We are now studying in more detail the flux tubes, in particular for the pentaquark.

- We will soon have codes for SU(2), SU(3), SU(4), etc, available on our webpage,

  http://nemea.ist.utl.pt/~ptqcd/

.

.

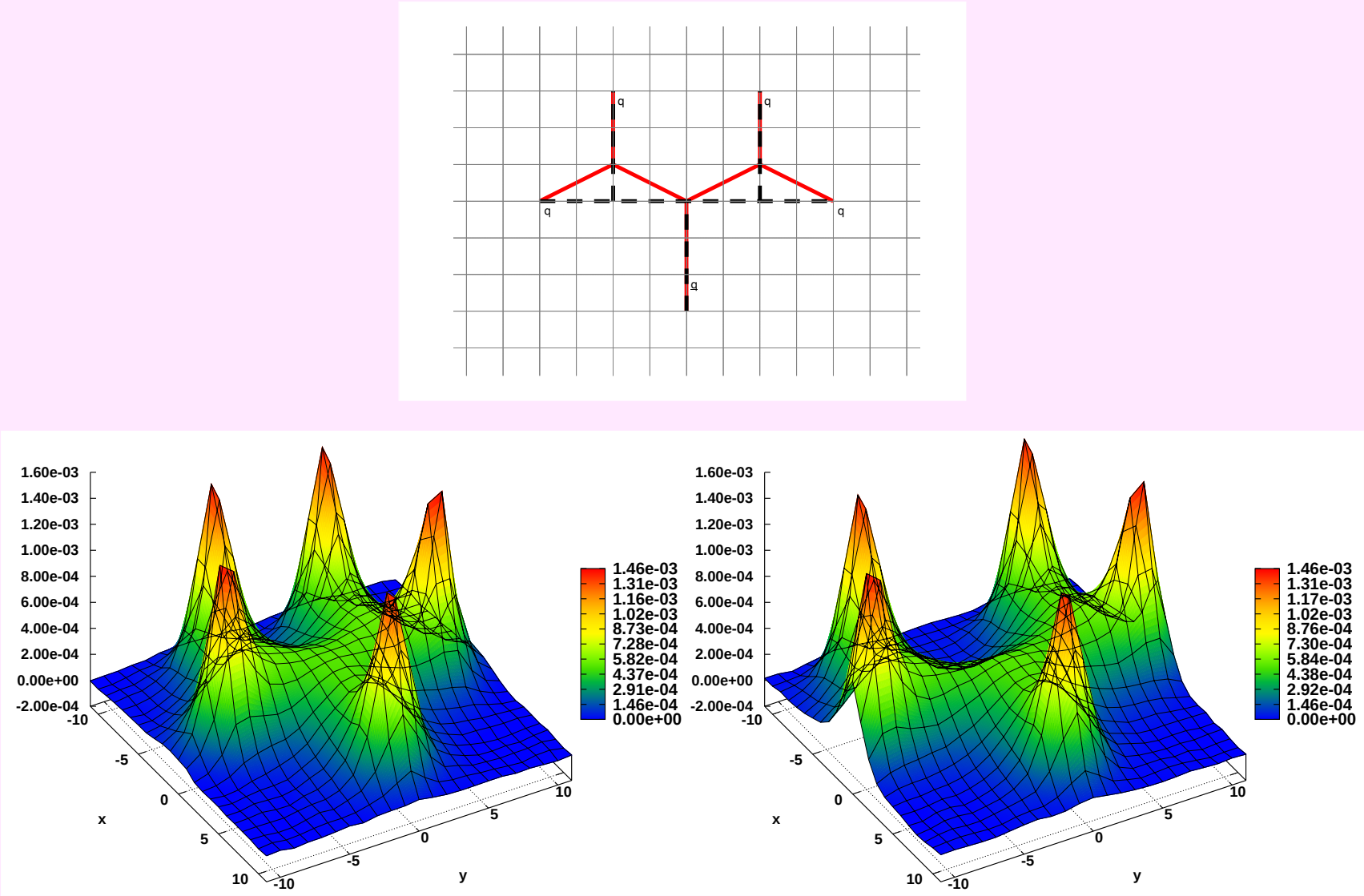

Figure 17: Wilson loop geometry, and preliminary result for the field, (Lagrangian density) for the static pentaquark. The results are presented in lattice spacing units (colour online).

acknowledgments

This work was partly funded by the FCT contracts, PTDC/FIS/100968/2008, CERN/FP/109327/2009 and CERN/FP/116383/2010. Nuno Cardoso is also supported by FCT under the contract SFRH/BD/44416/2008.

References

[1] R. L. Jaffe, "Multi-Quark Hadrons. 1. The Phenomenology of (2 Quark 2 anti-Quark) Mesons," *Phys. Rev.*, vol. D15, p. 267, 1977.

[2] B. Collaboration, "Observation of two charged bottomonium-like resonances," 2011.

[3] M. W. Beinker, B. C. Metsch, and H. R. Petry, "Bound q**2 - anti-q**2 states in a constituent quark model," *J. Phys.*, vol. G22, pp. 1151–1160, 1996.

[4] S. Zouzou, B. Silvestre-Brac, C. Gignoux, and J. M. Richard, "FOUR QUARK BOUND STATES," *Z. Phys.*, vol. C30, p. 457, 1986.

[5] B. A. Gelman and S. Nussinov, "Does a narrow tetraquark c c anti-u anti-d state exist?," *Phys. Lett.*, vol. B551, pp. 296–304, 2003.

[6] J. Vijande, A. Valcarce, and J. M. Richard, "Stability of multiquarks in a simple string model," *Phys. Rev.*, vol. D76, p. 114013, 2007.

[7] M. Karliner and H. J. Lipkin, "A Diquark-Triquark Model for the KN Pentaquark," *Phys. Lett.*, vol. B575, pp. 249–255, 2003.

[8] P. Bicudo and M. Cardoso, "Tetraquark resonances with the triple flip-flop potential, decays in the cherry in a broken glass approximation," *Phys. Rev.*, vol. D83, p. 094010, 2011.

[9] C. Alexandrou and G. Koutsou, "The static tetraquark and pentaquark potentials," *Phys. Rev.*, vol. D71, p. 014504, 2005.

[10] F. Okiharu, H. Suganuma, and T. T. Takahashi, "The tetraquark potential and flip-flop in SU(3) lattice QCD," *Phys. Rev.*, vol. D72, p. 014505, 2005.

[11] V. Bornyakov, P. Boyko, M. Chernodub, and M. Polikarpov, "Interactions of confining strings in SU(3) gluodynamics," 2005.

[12] P. Bicudo and M. Cardoso, "Iterative method to compute the Fermat points and Fermat distances of multiquarks," *Phys. Lett.*, vol. B674, pp. 98–102, 2009.

[13] J.-M. Richard, "Steiner-tree confinement and tetraquarks," 2009.

[14] H. Ichie, V. Bornyakov, T. Streuer, and G. Schierholz, "Flux tubes of two- and three-quark system in full QCD," *Nucl. Phys.*, vol. A721, pp. 899–902, 2003.

[15] F. Okiharu and R. M. Woloshyn, "An alternate smearing method for Wilson loops in lattice QCD," *Eur. Phys. J.*, vol. C35, pp. 537–542, 2004.

[16] M. Cardoso, N. Cardoso, and P. Bicudo, "Lattice QCD computation of the colour fields for the static hybrid quark-gluon-antiquark system, and microscopic study of the Casimir scaling," *Phys. Rev.*, vol. D81, p. 034504, 2010.

[17] N. Cardoso, M. Cardoso, and P. Bicudo, "Gauge invariant SU(3) lattice computation of the dual gluon mass and of the dual Ginzburg-Landau parameters λ and ξ in QCD," 2010.

[18] N. Cardoso and P. Bicudo, "SU(2) Lattice Gauge Theory Simulations on Fermi GPUs," *J. Comput. Phys.*, vol. 230, pp. 3998–4010, 2011.

[19] PTQCD, 2011. the CUDA codes are available at Portuguese Lattice QCD collaboration, `http://nemea.ist.utl.pt/~ptqcd`.

[20] A. Hasenfratz and F. Knechtli, "Flavor symmetry and the static potential with hypercubic blocking," *Phys. Rev. D*, vol. 64-3, p. 034504, 2001.

[21] N. Cardoso, M. Cardoso, and P. Bicudo, "Colour Fields Computed in SU(3) Lattice QCD for the Static Tetraquark System," 2011.